Geochemical Perspectives Letters

Silicate and iron phosphate melt immiscibility promotes REE enrichment

S.C. Yan, B. Wan, M. Anenburg, J.A. Mavrogenes

Supplementary Information

The Supplementary Information includes:

1. Rationale for Starting Compositions

Most natural immiscible Fe-rich melts contain 15–40 wt. % SiO_2 (Kamenetsky *et al.*, 2013). Fe-Si immiscibility is widely used to explain the formation of planetary metallic cores, iron oxide apatite deposits, Fe-Ti-P rich rocks, nelsonites, volcanic rocks and the Daly Gap, and layered intrusions (Charlier *et al.*, 2011; Veksler & Charlier, 2015; Fischer *et al.*, 2016; Yokoo *et al.*, 2022; Tornos *et al.*, 2024). Fe-Si immiscibility tends to occur in iron-rich systems, and the miscibility gap is widened by higher oxygen fugacity, phosphate, fluoride, water contents, and lower temperatures (Kamenetsky *et al.*, 2013; Lester *et al.*, 2013; Hou *et al.*, 2018; Lledo *et al.*, 2020). Therefore, we aimed for relatively high oxygen fugacity, iron phosphate, and water contents to match wide immiscibility conditions for Si- and FeP-rich melts.

2. Piston Cylinder Experiments

2.1 Preparation of Starting Materials

Powders of felsic silicate, FeP, and FeP-F compositions (FeP liquid + 7.3 CaF_2 wt. %) were synthesised using high-purity chemicals (Table S-1). Precision balance was used to accurately weigh all chemicals. All chemicals except FeO(OH) and $Al(OH)_3$ were mixed in acetone using an agate mortar and pestle. The mixed powder was made into a pellet and fired at 500 °C for 1 hour in a box furnace to remove CO_2 in Na_2CO_3 and K_2CO_3. Finally, the pellet was crushed to powder and mixed with FeO(OH) and $Al(OH)_3$ to add H_2O. The trace elements powder contains ~60 wt. % SiO_2 and 40 wt. % of most other elements of the periodic table in roughly equal proportions.

Table S-1 Chemicals used, and compositions of starting materials. Here, $D^{LFeP–LSi}$ values represent the elemental ratios between starting FeP and felsic silicate mix, which were used for plotting in Figure 3 in the main text.

Starting felsic silicate mix					Starting FeP mix*				
Chemicals (mg)		Oxides (mg)		wt. %	Chemicals (mg)		Oxides (mg)		wt. %	$D^{LFeP–LSi}$
SiO_2	680	SiO_2	680	66.67	SiO_2	46	SiO_2	46	4.51	0.07
TiO_2	10	TiO_2	10	0.98	TiO_2	15	TiO_2	15	1.47	1.5
$Al(OH)_3$#	137.7	Al_2O_3	90	8.82	$Al(OH)_3$#	79.6	Al_2O_3	52	5.09	0.58
Fe_2O_3	50	Fe_2O_3	50	4.90	FeO(OH)#	36.1	Fe_2O_3	346.8	33.97	6.93
MnO	10	MnO	10	0.98	MnO	31	MnO	31	3.04	3.1
MgO	10	MgO	10	0.98	MgO	50	MgO	50	4.90	5.0
$3CaO·P_2O_5$	20.3	CaO	11	1.08	$3CaO·P_2O_5$	92.2	CaO	50	4.90	4.54
$Na_2O·CO_2$'	34.2	Na_2O	20	1.96	$Na_2O·CO_2$'	30.8	Na_2O	18	1.76	0.90
$K_2O·CO_2$'	58.7	K_2O	40	3.92	$K_2O·CO_2$'	13.2	K_2O	9	0.88	0.22
		P_2O_5	9.28	0.91			P_2O5	321.8	31.52	34.65
					$Fe_2O_3·P_2O_5$	594				
CaF_2	2	F	0.97	0.10	CaF_2	10	F	4.9	0.48	5.05
		Ca	1.03	0.10			Ca	5.1	0.50	4.95
		H_2O	47.72	4.68			H_2O	31.2	3.06	0.65
Trace elements	20	Trace elements	20	1.96	Trace elements	20	Trace elements	20	1.96	1.0
V_2O_5	10	V_2O_5	10	0.98	V_2O_5	10	V_2O_5	10	0.98	1.0
Sc_2O_3	10	Sc_2O_3	10	0.98	Sc_2O_3	10	Sc_2O_3	10	0.98	1.0
Sum	1052.9	Sum	1020.0		Sum	1037.8	Sum	1020.8		
		CO_2'	32.9				CO_2'	17.0		

* FeP-F mix = FeP mix + 7.3 CaF_2 wt. %.
# OH^- bearing chemicals added after firing CO_2' at 500 °C for 1 hour in furnace.
' CO_2 was fired, so the final mixes do not contain CO_2.

2.2 High Temperature and Pressure Experiments

To prepare capsules, a noble metal tube was cut and welded on one side. Capsule materials are Pt, except $Au_{80}Pd_{20}$ for run 22, and $Au_{20}Pd_{80}$ for runs 20 and 39. Different layers (Table S-1) were weighed by precision balance and added into the capsule, followed by welding of the other side of the tube. Cylindrical assemblies of 5/8-inch NaCl sleeve, Pyrex, graphite, MgO, and the capsule were put into the piston cylinder apparatus to start the experiment. The temperature was monitored using type B thermocouple. Initial heating rate was 150 °C/min. Experiments were terminated by quenching to room temperature in 10–15 seconds. The capsules were then removed from the assembly and mounted in epoxy for polishing and further observations and geochemical analyses.

3. Microscope, EDS and Raman Analyses

Optical microscope and scanning electron microscope (SEM) were used to obtain optical and back-scattered electron (BSE) images and identify the experimental phase assemblages. A Zeiss Gemini450 and Nova NanoSEM 450 at the Institute of Geology and Geophysics, Chinese Academy of Sciences (IGGCAS), and a Hitachi 4300 at the Centre for Advanced Microscopy (CAM), the Australian National University were used, operating at ~15 kV and a beam current of ~1–2 nA. Raman spectroscopy was carried out at RSES, ANU, using a Horiba LabRAM Soleil spectrometer.

Magnetite and hematite were identified under reflected light by their different colour and extinction character in polarised light (*e.g.*, magnetite has complete extinction), as well as their Raman spectra (Fig. S-1). Apatite and whitlockite were identified by energy dispersive spectrometry (EDS) semi-quantifying the relative Ca and P content, as apatite contains more Ca than P, whereas whitlockite contains more P than Ca (Fig. S-2). Microstructures of quenched melts can be observed by high resolution BSE imaging. EDS analyses showed minor Fe absorption of capsules (Fig. S-3). Experimental textures of runs not shown in the main text are given in Figure S-4.

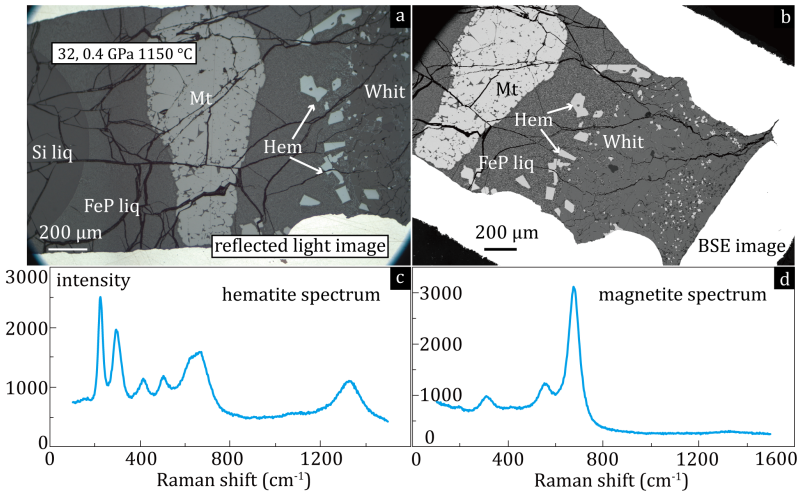

Figure S-1 Identification of magnetite and hematite. Large grains show **(a)** different colours in reflected light, **(b)** almost indistinguishable brightness under BSE image**,** and **(c, d)** distinct Raman spectra. Identification is more difficult for tiny µm-scale grains.

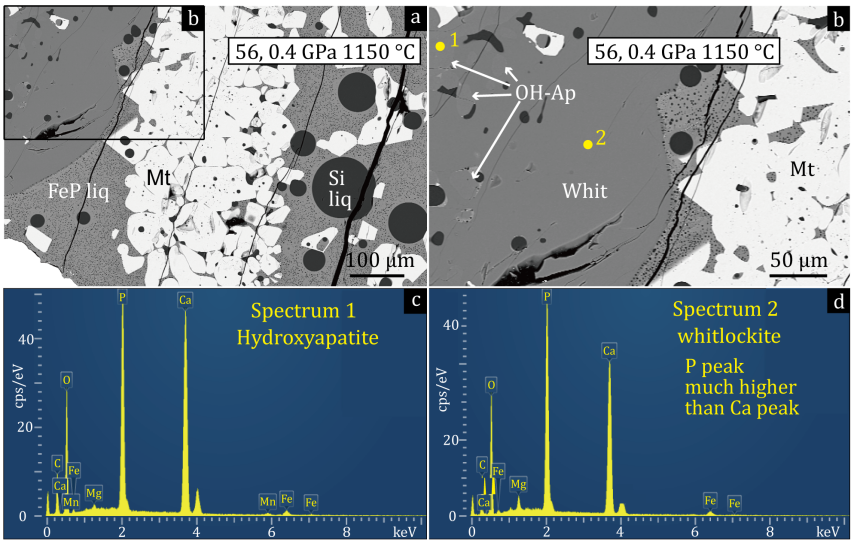

Figure S-2 Identification of apatite and whitlockite by **(a, b)** minor differences in BSE brightness and **(c, d)** contrasting EDS spectra.

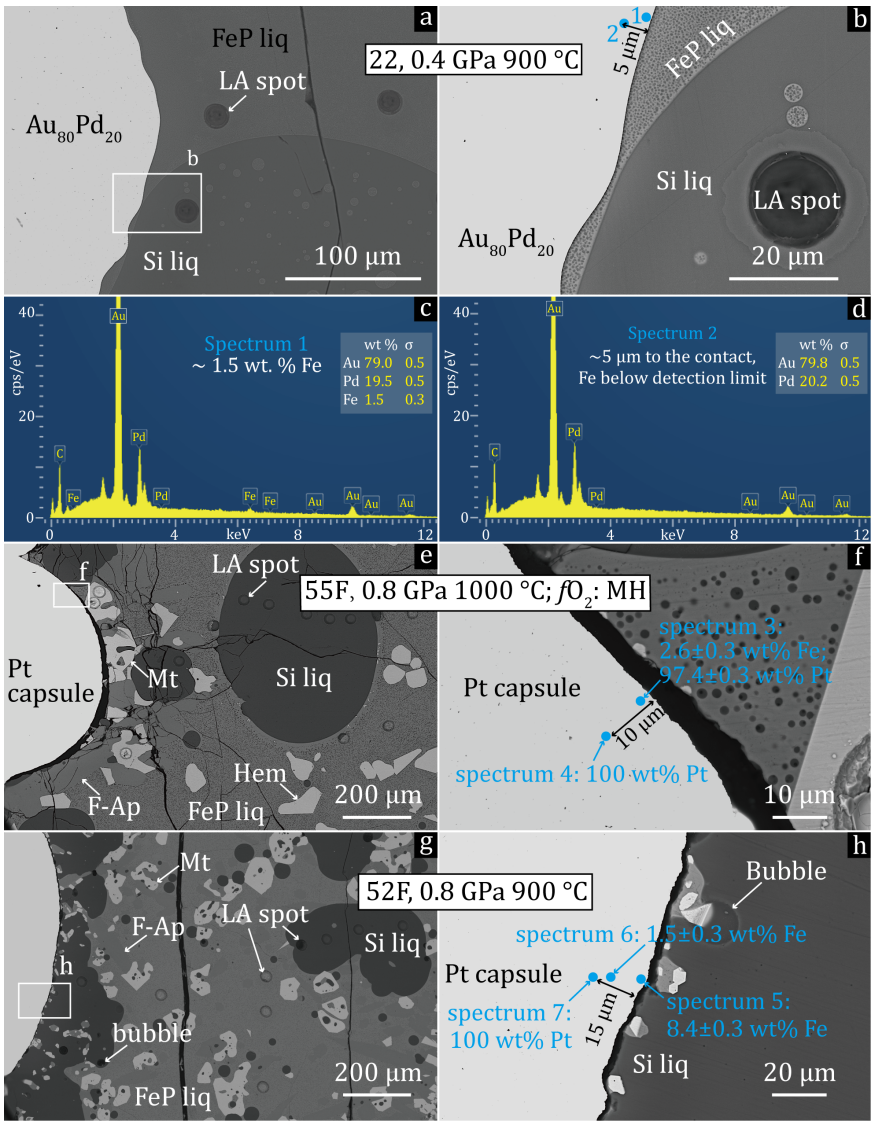

Figure S-3 **(c, d, f, h)** Fe absorption by capsule materials as shown by EDS analyses; panels **(a, b, e, g)** indicate areas of analyses. The most severe case shown in h, where Fe content reaches up to ~8.4 wt. % at the capsule-experiment contact, whereas it is below detection limit at ~15 µm from the contact.

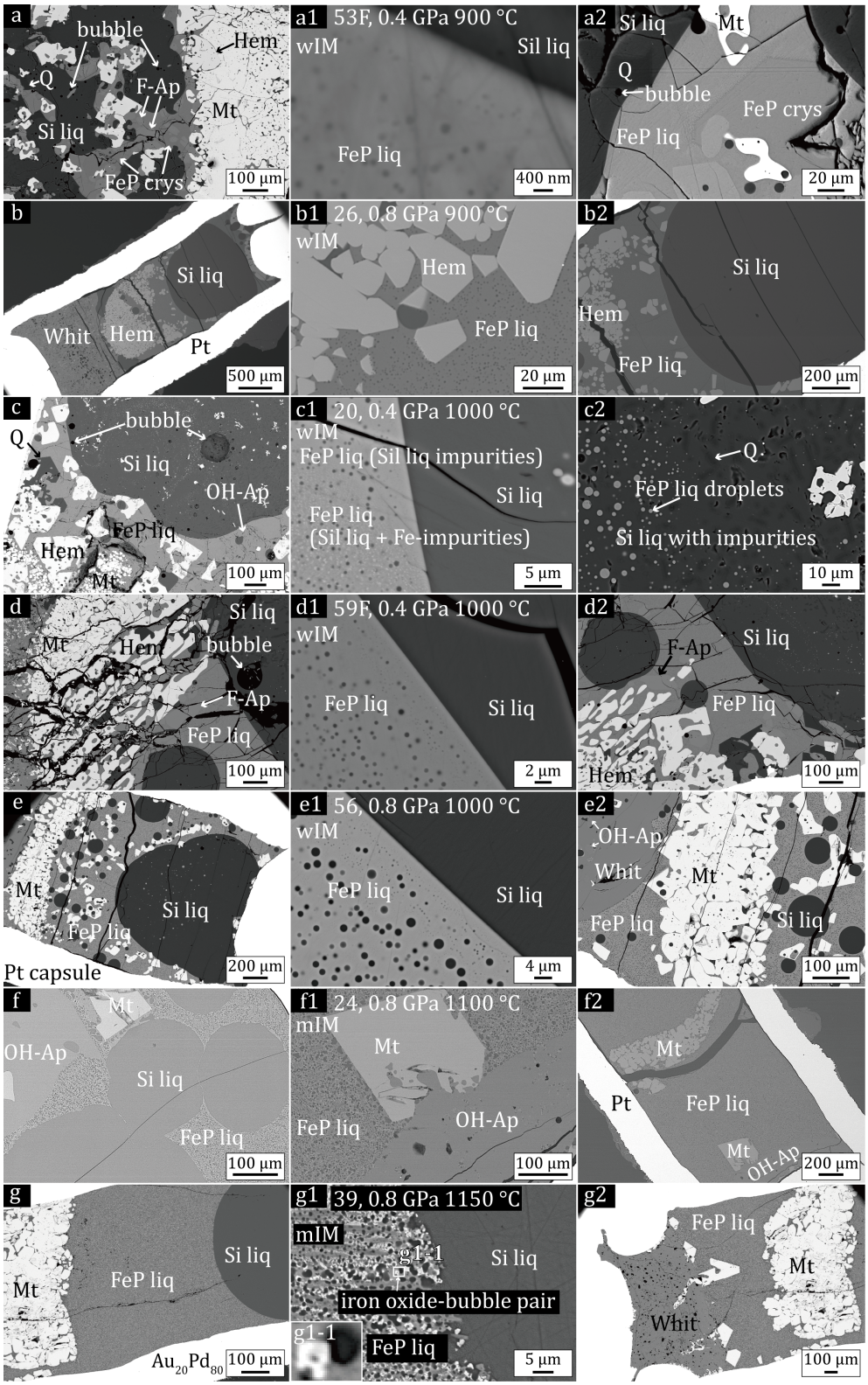

Figure S-4 BSE images of seven runs not shown in main text, with run conditions listed in **(a1-f1)**. Abbreviations: Q, quartz; Hem, Hematite; Mt, magnetite; Si liq, silicate liquid; crys, crystal; F-Ap, fluorapatite; OH-Ap, hydroxyapatite; Whit, whitlockite; Pt, Platinum; nIM, narrow immiscibility; mIM, moderate immiscibility; wIM, wide immiscibility.

4. Major Element Analyses

Major elements of all synthetic immiscible FeP- and Si-rich liquids and FeP crystals were analysed by wavelength-dispersive spectrometry (WDS) on a JEOL JXA-8100 electron probe microanalyser at IGGCAS, with an accelerating voltage of 15 kV and a beam current of 20 nA. Spot size diameters were 20 μm, except for 5 μm in cases of small FeP liquids in runs 57F and 58F. For glasses, three to seven points (Fig. S-5) were measured and presented as average in the main text. Natural minerals and synthetic oxides were used as standards, and the ZAF procedure was used for matrix corrections.

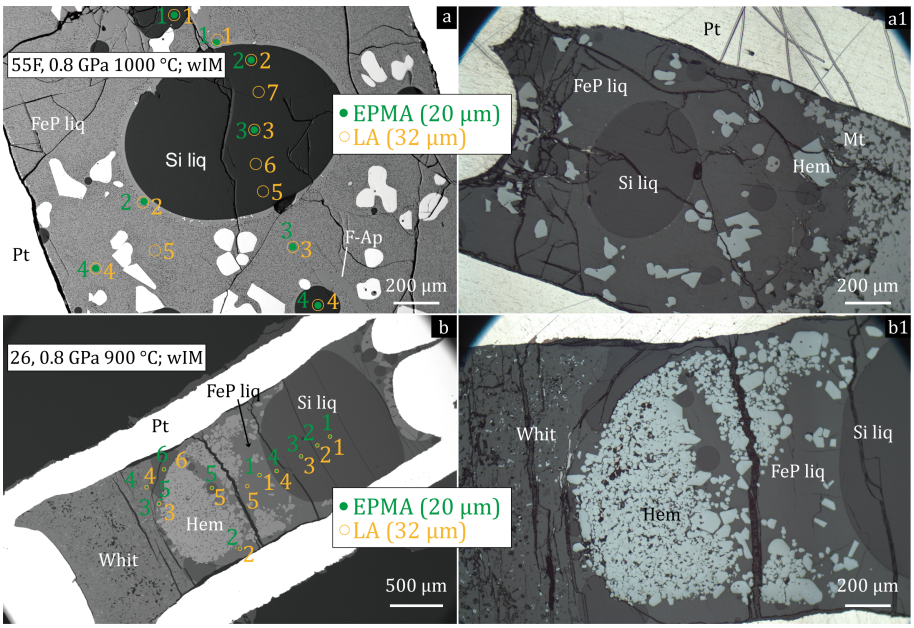

Figure S-5 Examples of analytical locations, shown by **(a–a1)** run 55F and **(b–b1)** run 26, that contain different melt pools. Abbreviations same as Figure S-4. Left panels are BSE images, and right panels are optical reflected light photographs.

5. Trace Element Analyses

Except for runs 57F and 58F, which contain liquid pools too small to measure, all runs were measured for trace elements in quenched melts. Run 20 has FeP liquids with two different kinds of impurities (*e.g.*, Si liquid droplets and unidentified Fe-rich droplets; Fig. S-4c1) and Si-rich liquids with many tiny impurities (*e.g.*, quartz and FeP droplets; Fig. S-4c2),

making trace element data inconsistent between repeat analyses, hence run 20 was not used for partition coefficient (*D*) calculation. For each quenched melt, three to eight points were measured (Fig. S-5). Trace element abundances of the immiscible FeP- and Si-rich melts were determined by laser ablation-inductively coupled plasma-mass spectrometry (LA-ICP-MS) employing an Element XR HR-ICP-MS instrument (Thermo Fisher Scientific, USA) coupled to an Analyte G2 193 nm ArF excimer laser ablation system at the State Key Laboratory of Lithospheric and Environmental Coevolution, IGGCAS. The approach is similar to that outlined in Wu *et al.*, (2018a) with isotopes measured using a peak-hopping mode with a laser diameter of ~32 μm and 3 Hz repetition rate. For run 22, the diameter is of ~16 μm with a 5 Hz repetition rate. The laser energy density is ~4.0 J/cm^2. The Element XR is equipped with a jet-interface, comprising of a jet sample cone, an X-version skimmer cone and a high-capacity vacuum pump (OnTool Booster 150, Asslar, Germany). This leads to a signal enhancement in laser sampling mode by a factor of 3–5, resulting in an improved detection capability. Helium was employed as the ablation gas to improve the transporting efficiency of ablated aerosols. NIST SRM 610 reference glass was used for external calibration and ARM-1 (Wu *et al.*, 2019) and OJY-1 glass were used for quality control monitoring. Calcium (^{43}Ca) was used as an internal standard. The resulting data were reduced using the Iolite program with the bulk normalisation as 100 % (m/m) (Wu *et al.*, 2018b). In the few cases where deeply buried impurities were encountered, their presence was identified in the time-resolved signal and readily removed before data processing. For most trace elements (>0.005 μg/g), the accuracy is better than ±10 % with analytical precision (1 RSD) of ±10 %. Occasionally, negative values or values of 2 RSD above 100 % are below the detection limit and not used (*e.g.*, Fig. 3).

Table S-2 Summary of melt major elements based on average compositions for each experiment.

	SiO_2	Al_2O_3	P_2O_5	FeOt	MgO	CaO	Na_2O	TiO_2	K_2O	F'	MnO	Total*
nIM Si liq	55.0–55.9	10.4–10.8	5.5–6.3	15.3–15.9	0.8–1.0	4.7–5.0	4.9–5.8	0.4–0.6	0.06–0.14		0.4–0.6	99.0–100.6
nIM FeP liq	28.5–31.9	5.8–6.5	16.7–19.6	26.5–27.1	1.9–2.1	10.8–11.9	3.1–3.6	0.8–0.9	0.02–0.05		1.0–1.1	100.5–100.6
mIM Si liq	54.5–63.6	8.1–10.3	2.2–7.4	4.3–13.2	0.3–0.8	0.8–4.8	4.1–5.6	0.2–0.5	0.04–0.09		0.2–0.4	92.3–94.0
mIM FeP liq	13.6–26.3	3.9–5.3	21.4–33.0	21.2–29.1	1.9–4.2	10.8–17.5	3.0–3.4	0.3–1.2	0.02–0.04		0.9–1.8	94.6–98.6
wIM Si liq	63.6–74.9	10.2–13.7	1.2–4.1	1.5–4.8	0.1–0.4	0.1–0.8	4.9–6.6	0.04–0.4	0.05–0.08	0.6	0.07–0.19	89.0–99.3
wIM FeP liq	2.3–7.0	0.4–7.9	36.3–43.1	17.0–34.9	4.7–9.7	4.0–13.7	2.9–5.8	0.08–0.9	0.01–0.04	0.9–3.2	2.0–3.5	94.3–101.7

' Only show F concentrations of 53F, 57F, and 58F, as their liquids contain minimal impurities.
* Totals below 100 wt. % mainly due to nm–μm epoxy bubbles and H_2O in the resultant glass (*e.g.*, Fig. 2e).

6. Geochemical Characteristics

Major elements of all synthesised liquids and FeP crystals are shown in Figures 1, 3 and Table S-2, with detailed data present in Dataset S-1. Trace elements and *D* values of 11 runs (Fig. 3d) are summarised in Dataset S-2, and the point-by-point data are listed in Datasets S-3 to S-12.

7. Equilibrium of Experiments

Figure S-6 shows that three representative runs of different immiscible degree all have consistent major and trace element concentrations, showing the equilibrium between two immiscible melts. Although the Ce(max/min) of silicate liquids from 56 and 47F—used as a proxy for the REE—show variation from 1.5–1.9 (Table 1), their elements are generally consistent (Fig. S-7), hence their immiscible melts are still thought to be well equilibrated. Relationship between temperature and $D^{LFeP–LSi}$ values further demonstrates adequate chemical exchange and equilibrium between the resultant immiscible FeP and silicate liquids in our experiments (Fig. S-8). Elemental variations of runs 53F, 54F, and 59F, deriving their complex "semi equilibrated" status, were shown in Figures S-9 and S-10.

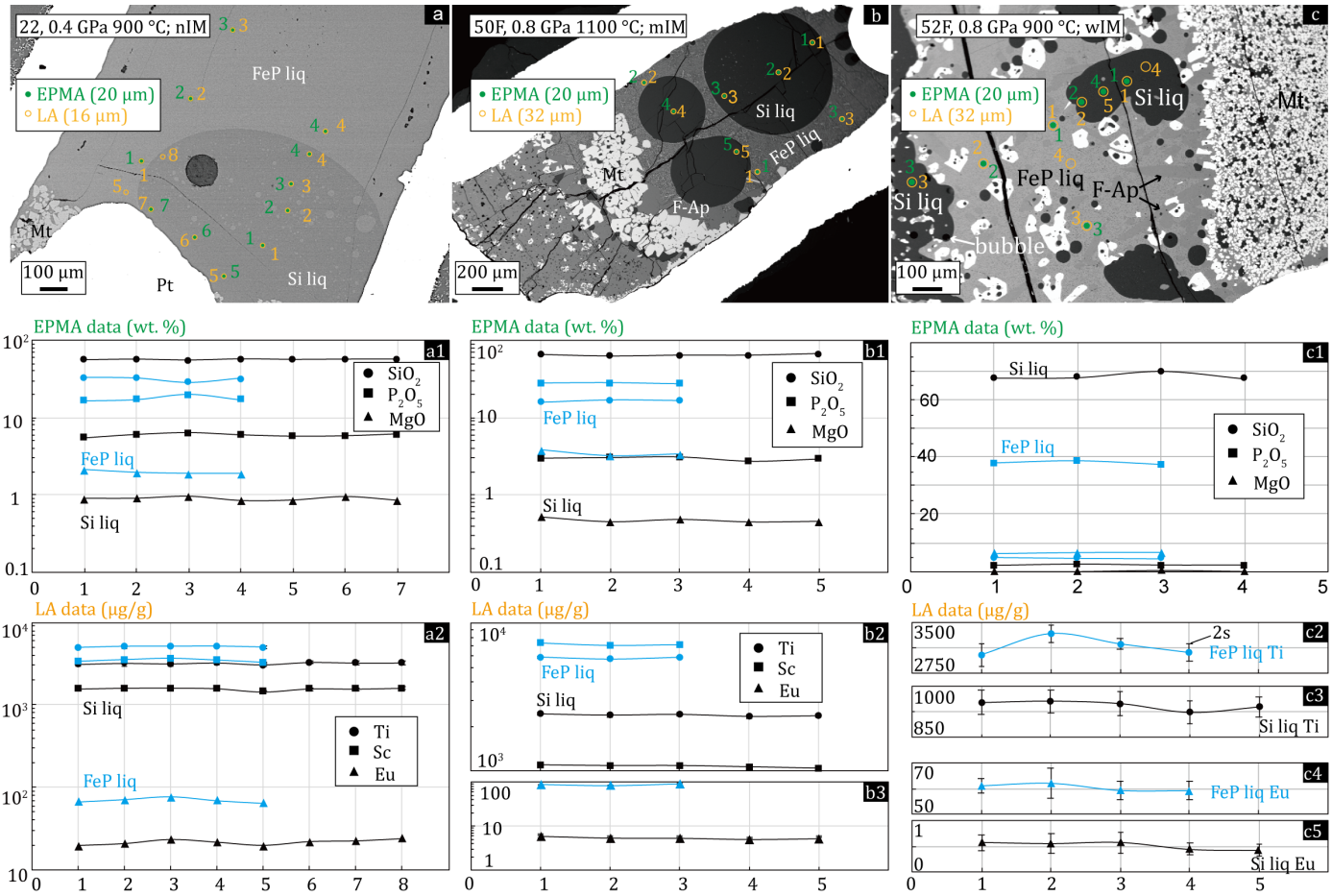

Figure S-6 Consistent major and trace element contents from runs of different immiscibility degree showing the equilibrium between two melts. **(a–a2)** run 22; **(b–b3)** run 50F; **(c–c5)** run 52F. Abbreviations are as in Figure S-4.

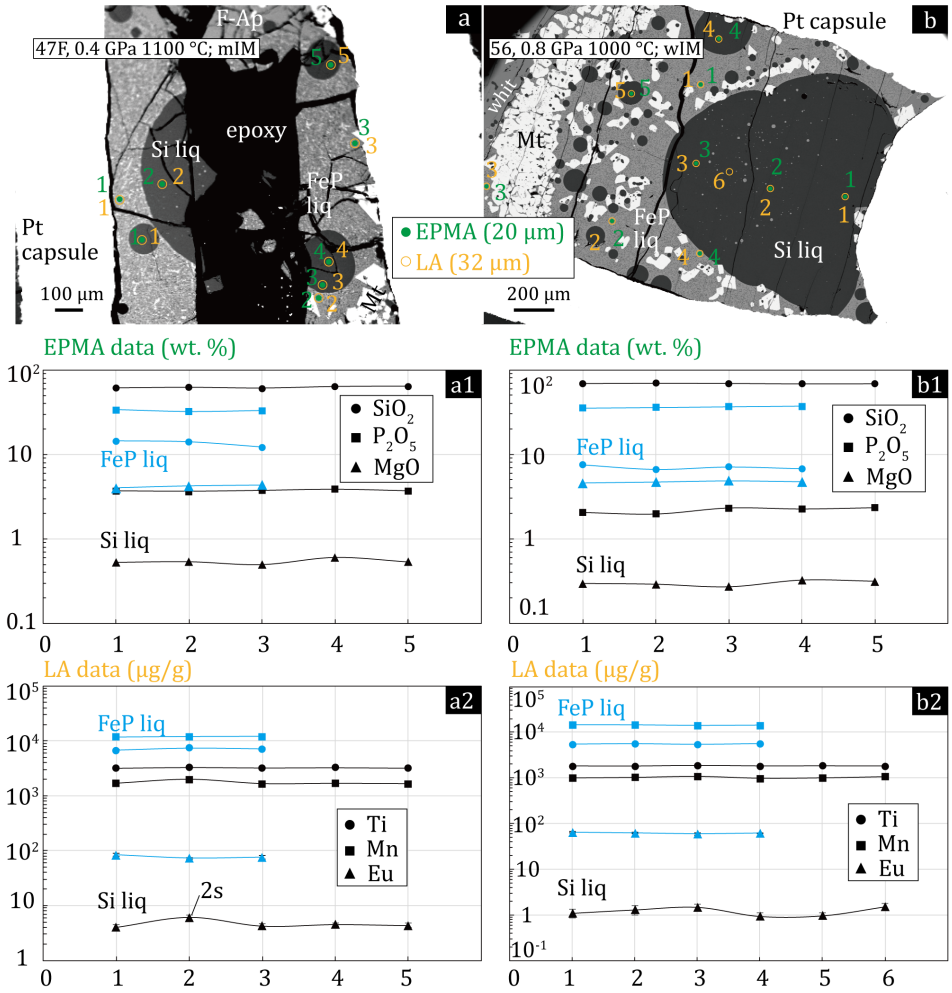

Figure S-7 General consistent element contents of **(a–a2)** run 47F and **(b–b2)** run 56. Abbreviations same as Figure S-4.

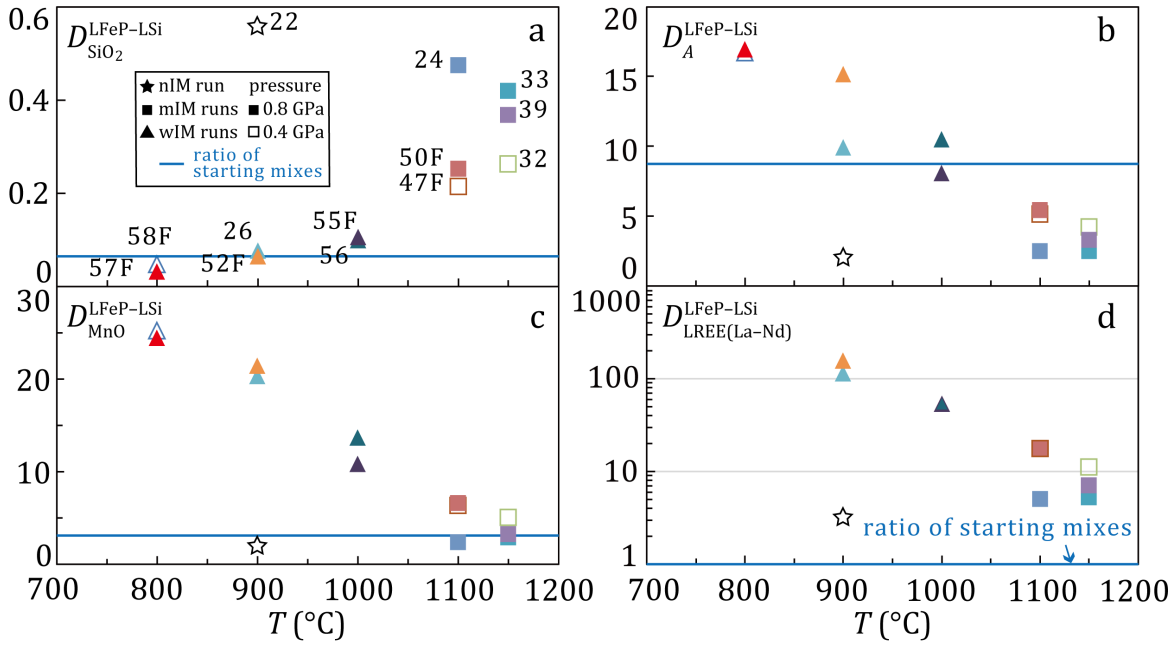

Figure S-8 $D^{\text{LFeP–LSi}}$ values *versus* temperature, showing immiscible liquids of wIM and mIM runs have compositions different from starting compositions and their $D^{\text{LFeP–LSi}}$ values are temperature dependent, supporting adequate chemical exchange and equilibrium between the resultant FeP and silicate liquids. In **(b)**, $A = TiO_2 + FeO_{total} + MgO + CaO + P_2O_5$ (wt. %). Runs 57F and 58F are plotted for comparison.

For runs 53F, both 16 μm spot and 32 μm spot LA data were plotted for reference. *D* values of runs 53F, 54F, and 59F are not discussed due to the half-equilibrium status. In detail, for wIM runs 53F, 54F, and 59F, we found consistent elemental compositions for FeP liquids (Figs. S-9, S-10). For the Si liquids, elements such as Mn, Rb, Sr, Li, Mg, K, Fe, Co, Cu, Zn, Ge, Ag, Cs, Ba, Pb were consistent across spatially separated analyses and therefore considered to be equilibrated with FeP liquids. Trace elements such as the REE also demonstrate relatively good equilibrium. For example, Ce concentrations were mostly consistent for Si liquids. The worst-case scenario is in experiment 53F where Ce contents of silicate droplets varied from 1.16 to 6.33 μg/g (factor of 5.5) between different analytical spots within the same phase (Table 1). This difference is negligible relative to the Ce ratios between FeP and silicate liquids (Fig. 3e), and inter-experiment variability. Some elements in Si liquids (*e.g.,* Ti, Nb, Ta) exhibited substantial variability for runs 53F, 54F, and 59F (Figs. S-9, S-10). Considering this semi-equilibrium condition, *D* values of these three runs are excluded from discussion. Runs 57F and 58F yielded dendritic magnetite, indicating that the Fe-oxide liquids are depolymerised and crystallise during quench. Liquids of runs 20, 57F and 58F are too small for LA analyses, hence demonstration of elemental consistency is challenging, and *D* values are not discussed.

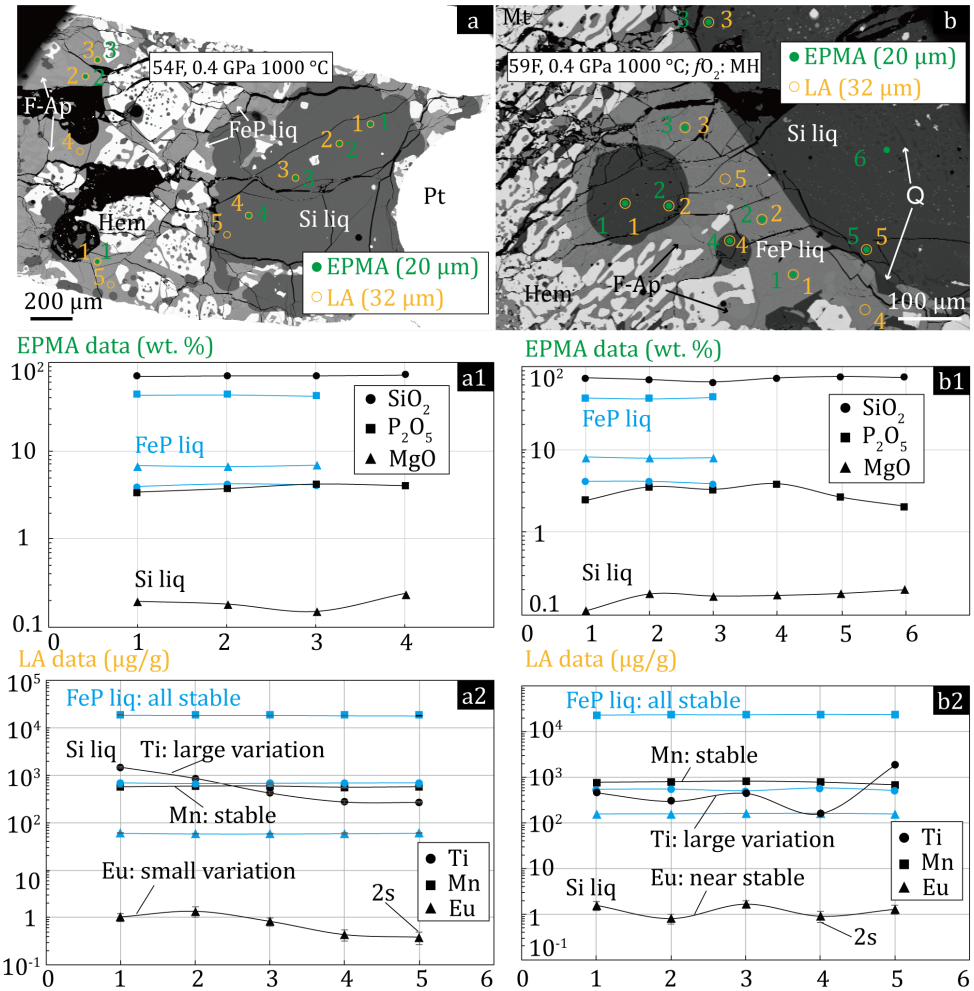

Figure S-9 Elemental variations of **(a–a2)** run 54F and **(b–b2)** 59F. Major elements are generally consistent, while trace elements show either consistent, large, or small variations. Abbreviations same as Figure S-4.

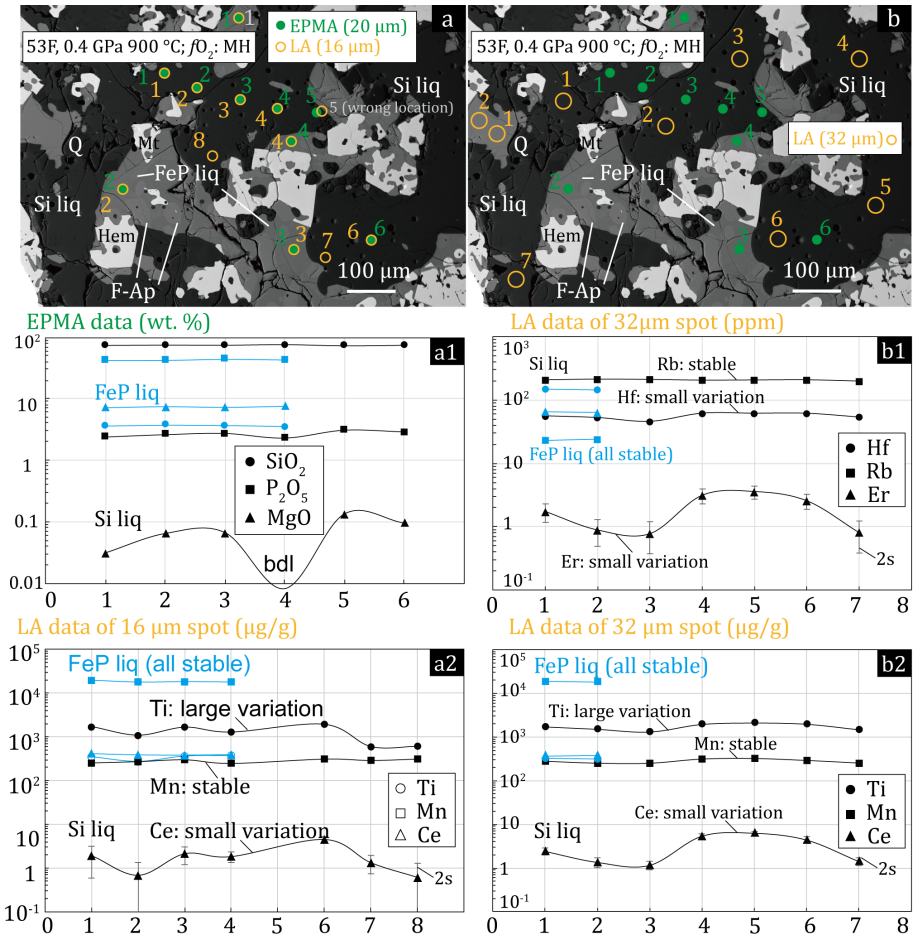

Figure S-10 Elemental variations of run 53F. Major elements are generally consistent, while trace elements show either consistent, large, or small variation for both **(a–a2)** 16 µm and **(b–b2)** 32 µm spots. Abbreviations same as Figure S-4.

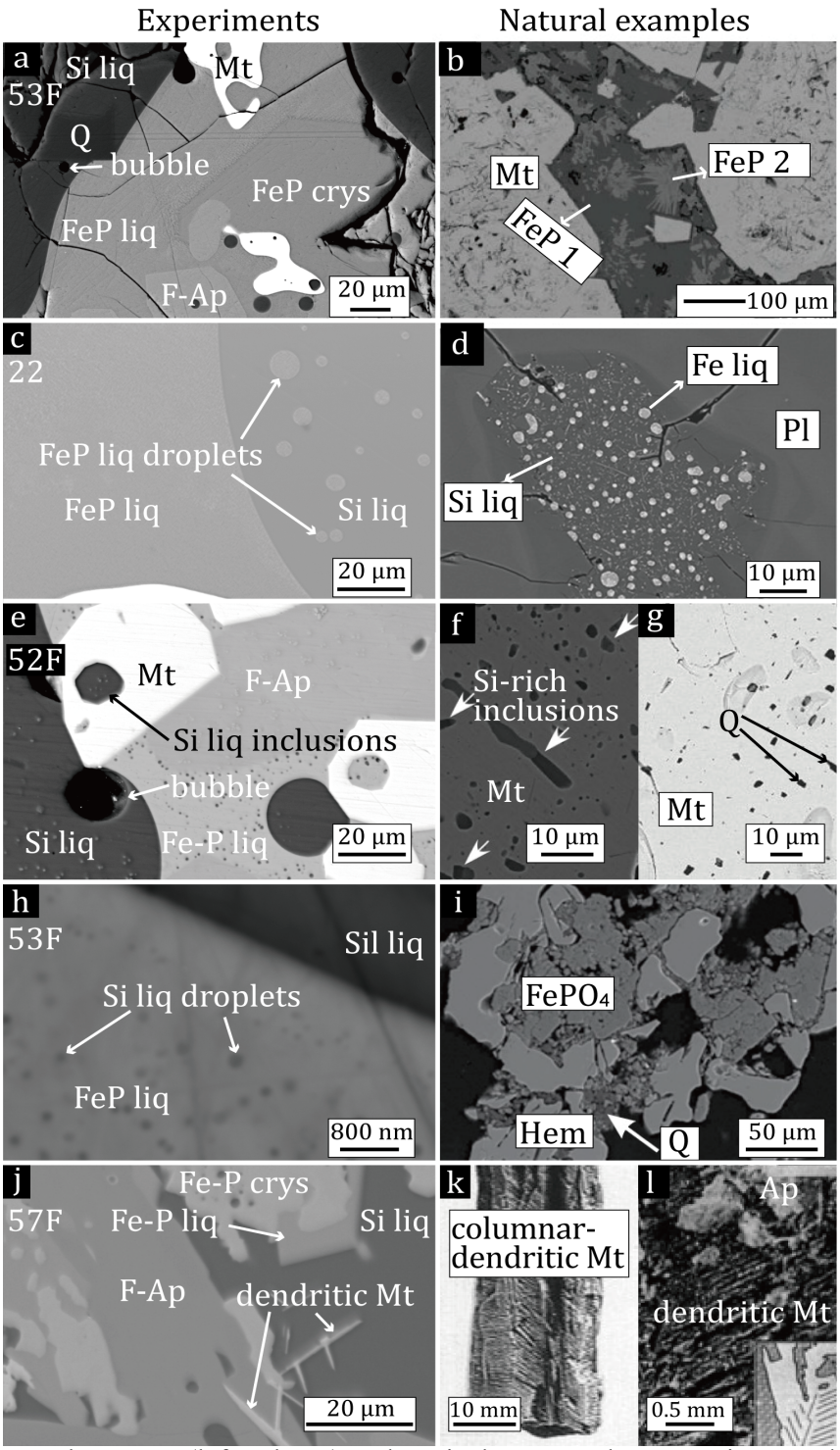

Figure S-11 Experimental textures (left column) and equivalent natural textures in IOA deposits (right column), shown by **(a, b)** two FeP phases, **(c, d)** FeP liq droplets surrounded by Si liquids, **(e–g)** Si-rich inclusions or quartz inside magnetite, **(h, i)** Si liquid droplets or quartz in FeP phases, and **(j–l)** dendritic magnetite. References: **(b)** El Laco (Xie *et al.*, 2019); **(d)** El Laco (Velasco *et al.*, 2016); **(f)** El Laco (Tornos *et al.*, 2024); **(g)** El Romeral (Rojas *et al.*, 2018); **(i)** El Laco (Mungall *et al.*, 2018); **(k)** El Laco (Nyström and Henríquez, 1994); **(l)** Kiruna (Nyström and Henriquez, 1989). Abbreviations: Pl, plagioclase; others same as Figure S-4.

Supplementary Datasets

Dataset S-1 Major elements of glasses.
Dataset S-2 Trace elements of glasses and *D* values.
Dataset S-3 Trace elements of Run 22_ARM-1 (16 µm).
Dataset S-4 Trace elements of Run 39_ARM-1.
Dataset S-5 Trace elements of Runs 26 52F_ARM-1.
Dataset S-6 Trace elements of Runs 32 33_ARM-1.
Dataset S-7 Trace elements of Runs 50F 24_ARM-1.
Dataset S-8 Trace elements of Runs 56 47F_ARM-1.
Dataset S-9 Trace elements of Runs 59F 55F_ARM-1.
Dataset S-10 Trace elements of Runs 20 54F_ARM-1.
Dataset S-11 Trace elements of Run 53F_ARM-1 (16 µm; for reference only).
Dataset S-12 Trace elements of Run 53F_ARM-1 (32 µm; for reference only).

Datasets S-1 and S-2 (.xlsx) and S-3 to S-12 (.xlsx files in a single .zip directory) are available for download (.xlsx) from the online version of this article at http://doi.org/10.7185/geochemlet.2436.

Supplementary Information References

Charlier, B., Namur, O., Toplis, M.J., Schiano, P., Cluzel, N., *et al.* (2011) Large-scale silicate liquid immiscibility during differentiation of tholeiitic basalt to granite and the origin of the Daly gap. *Geology* 39, 907–910. https://doi.org/10.1130/g32091.1

Fischer, L.A., Wang, M., Charlier, B., Namur, O., Roberts, R.J., *et al.* (2016) Immiscible iron- and silica-rich liquids in the Upper Zone of the Bushveld Complex. *Earth and Planetary Science Letters* 443, 108–117. https://doi.org/10.1016/j.epsl.2016.03.016

Hou, T., Charlier, B., Holtz, F., Veksler, I., Zhang, Z., *et al.* (2018) Immiscible hydrous Fe–Ca–P melt and the origin of iron oxide-apatite ore deposits. *Nature Communications* 9, 1415. https://doi.org/10.1038/s41467-018-03761-4

Kamenetsky, V.S., Charlier, B., Zhitova, L., Sharygin, V., Davidson, P., Feig, S. (2013) Magma chamber-scale liquid immiscibility in the Siberian Traps represented by melt pools in native iron. *Geology* 41, 1091–1094. https://doi.org/10.1130/g34638.1

Lester, G.W., Clark, A.H., Kyser, T.K., Naslund, H.R. (2013) Experiments on liquid immiscibility in silicate melts with H_2O, P, S, F and Cl: implications for natural magmas. *Contributions to Mineralogy and Petrology* 166, 329–349. https://doi.org/10.1007/s00410-013-0878-1

Lledo, H.L., Naslund, H.R., Jenkins, D.M. (2020) Experiments on phosphate–silicate liquid immiscibility with potential links to iron oxide apatite and nelsonite deposits. *Contributions to Mineralogy and Petrology* 175, 111. https://doi.org/10.1007/s00410-020-01751-8

Mungall, J.E., Long, K., Brenan, J.M., Smythe, D., Naslund, H.R. (2018) Immiscible shoshonitic and Fe-P-oxide melts preserved in unconsolidated tephra at El Laco volcano, Chile. *Geology* 46, 255–258. https://doi.org/10.1130/g39707.1

Nyström, J.O., Henriquez, F. (1989) Dendritic magnetite and miniature diapir-like concentrations of apatite: Two magmatic features of the Kiirunavaara iron ore. *GFF* 111, 53–64. https://doi.org/10.1080/11035898909454759

Nyström, J.O., Henriquez, F. (1994) Magmatic features of iron ores of the Kiruna type in Chile and Sweden; ore textures and magnetite geochemistry. *Economic Geology* 89, 820–839. https://doi.org/10.2113/gsecongeo.89.4.820

Rojas, P.A., Barra, F., Deditius, A., Reich, M., Simon, A., *et al.* (2018) New contributions to the understanding of Kiruna-type iron oxide-apatite deposits revealed by magnetite ore and gangue mineral geochemistry at the El Romeral deposit, Chile. *Ore Geology Reviews* 93, 413–435. https://doi.org/10.1016/j.oregeorev.2018.01.003

Tornos, F., Hanchar, J.M., Steele-MacInnis, M., Crespo, E., Kamenetsky, V.S., Casquet, C. (2024) Formation of magnetite-(apatite) systems by crystallizing ultrabasic iron-rich melts and slag separation. *Mineralium Deposita* 59, 189–225. https://doi.org/10.1007/s00126-023-01203-w

Veksler, I.V., Charlier, B. (2015) Silicate Liquid Immiscibility in Layered Intrusions. In: Charlier, B., Namur, O., Latypov, R., Tegner, C. (Eds.) *Layered Intrusions*. Springer, Dordrecht, 229–258. https://doi.org/10.1007/978-94-017-9652-1_5

Velasco, F., Tornos, F., Hanchar, J.M. (2016) Immiscible iron- and silica-rich melts and magnetite geochemistry at the El Laco volcano (northern Chile): Evidence for a magmatic origin for the magnetite deposits. *Ore Geology Reviews* 79, 346–366. https://doi.org/10.1016/j.oregeorev.2016.06.007

Wu, S., Karius, V., Schmidt, B.C., Simon, K., Wörner, G. (2018a) Comparison of Ultrafine Powder Pellet and Flux-free Fusion Glass for Bulk Analysis of Granitoids by Laser Ablation-Inductively Coupled Plasma-Mass Spectrometry. *Geostandards and Geoanalytical Research* 42, 575–591. https://doi.org/10.1111/ggr.12230

Wu, S.-T., Huang, C., Xie, L.-W., Yang, Y.-H., Yang, J.-H. (2018b) Iolite Based Bulk Normalization as 100% (*m*/*m*) Quantification Strategy for Reduction of Laser Ablation-Inductively Coupled Plasma-Mass Spectrometry Transient Signal. *Chinese Journal of Analytical Chemistry* 46, 1628–1636. https://doi.org/10.1016/s1872-2040(18)61118-1

Wu, S., Wörner, G., Jochum, K.P., Stoll, B., Simon, K., Kronz, A. (2019) The Preparation and Preliminary Characterisation of Three Synthetic Andesite Reference Glass Materials (ARM-1, ARM-2, ARM-3) for *In Situ* Microanalysis. *Geostandards and Geoanalytical Research* 43, 567–584. https://doi.org/10.1111/ggr.12301

Xie, Q., Zhang, Z., Hou, T., Cheng, Z., Campos, E., *et al.* (2019) New Insights for the Formation of Kiruna-Type Iron Deposits by Immiscible Hydrous Fe-P Melt and High-Temperature Hydrothermal Processes: Evidence from El Laco Deposit. *Economic Geology* 114, 35–46. https://doi.org/10.5382/econgeo.2019.4618

Yokoo, S., Hirose, K., Tagawa, S., Morard, G., Ohishi, Y. (2022) Stratification in planetary cores by liquid immiscibility in Fe-S-H. *Nature Communications* 13, 644. https://doi.org/10.1038/s41467-022-28274-z